

Structural, elastic and thermal properties of cementite (Fe_3C) calculated using Modified Embedded Atom Method

Laalitha S. I. Liyanage

*Department of Physics and Astronomy, Mississippi State University, Mississippi State, MS 39762, USA and
Center for Advanced Vehicular Systems, Mississippi State University, Mississippi State, MS 39762, USA*

Seong-Gon Kim*

*Department of Physics and Astronomy, Mississippi State University, Mississippi State, MS 39762, USA and
Center for Computational Sciences, Mississippi State University, Mississippi State, MS 39762, USA*

Jeff Houze and Sungho Kim

Center for Advanced Vehicular Systems, Mississippi State University, Mississippi State, MS 39762, USA

Mark A. Tschopp

Army Research Laboratory, Aberdeen Proving Ground, MD 21005, USA

M. I. Baskes

*Department of Mechanical and Aerospace Engineering,
University of California, San Diego, La Jolla, CA 92093, USA and
Los Alamos National Laboratory Los Alamos, NM 87545, USA*

M. F. Horstemeyer

*Department of Mechanical Engineering, Mississippi State University, Mississippi State, MS 39762, USA and
Center for Advanced Vehicular Systems, Mississippi State University, Mississippi State, MS 39762, USA*

(Dated: February 25, 2014)

Structural, elastic and thermal properties of cementite (Fe_3C) were studied using a Modified Embedded Atom Method (MEAM) potential for iron-carbon (Fe-C) alloys. Previously developed Fe and C single element potentials were used to develop a Fe-C alloy MEAM potential, using a statistically-based optimization scheme to reproduce structural and elastic properties of cementite, the interstitial energies of C in bcc Fe as well as heat of formation of Fe-C alloys in L_{12} and B_1 structures. The stability of cementite was investigated by molecular dynamics simulations at high temperatures. The nine single crystal elastic constants for cementite were obtained by computing total energies for strained cells. Polycrystalline elastic moduli for cementite were calculated from the single crystal elastic constants of cementite. The formation energies of (001), (010), and (100) surfaces of cementite were also calculated. The melting temperature and the variation of specific heat and volume with respect to temperature were investigated by performing a two-phase (solid/liquid) molecular dynamics simulation of cementite. The predictions of the potential are in good agreement with first-principles calculations and experiments.

PACS numbers: 61.50.Lt, 62.20.de, 61.72.jj, 68.35.Md, 71.15.Pd

I. INTRODUCTION

Steel alloys are the most widely used structural materials due to their abundance, all-purpose applicability and low cost. The main carbide in steel alloys is cementite, which forms a precipitate. Cementite has a direct impact on the mechanical, structural, and thermal properties of steel. Therefore the ability to describe and predict properties of cementite at the nanoscale is essential in the study and design of new steels. Atomistic simulation methods, such as molecular dynamics or Monte Carlo simulations, offer an efficient and reliable route to investigate nanoscale mechanics pertaining to cementite in steel alloys. Each of these methods requires accurate interatomic potentials to find the energy of the system under investigation. However, first-principles calculations—

albeit rigorous and accurate—are incapable of simulating a large number of atoms required for realistic calculations due to unreasonable memory and processing-time requirements. Therefore, semi-empirical potential methods are being explored as a suitable alternative.

Among the spectrum of semi-empirical formulations, the Modified Embedded Atom Method (MEAM)¹, originally proposed by Baskes et al., has been shown to accurately predict properties of most crystal structures, such as bcc, fcc, hcp, and even diatomic gases, in good agreement with experiments or first-principles calculations. MEAM is extended from the Embedded Atom Method (EAM)² to include the directionality of bonds. In the original MEAM formalism, only the first-nearest neighbor (1NN) interactions were considered.¹ Lee and Baskes later extended the original formalism to include the screened second-nearest neighbor (2NN) interactions.³

Further details of the MEAM formalism can be found in Ref. 1 and 3.

One of the commonly used 2NN MEAM potentials for the Fe-C system developed by Byeong-Joo Lee⁴ is designed to predict the interactions of interstitial C atoms with defects, such as vacancies. According to Fang et al.,⁵ Lee's potential predicts that cementite is only stable up to a temperature of 750 K.⁵ Experimentally, however, cementite is metastable with a positive heat of formation⁶ and only decomposes between 1100 and 1200 K.^{7,8} Among recent interatomic potentials⁸⁻¹² for the Fe-C system, EAM potentials by Lau et al.¹⁰ and Ruda et al.¹² and the short ranged Tersoff-Brenner type analytical bond order potential (ABOP) by Henriksson et al.⁸ all promise to predict properties of cementite reasonably well. In the potentials by Lau et al.¹⁰ and Ruda et al.,¹² however, the single element potential for C does not predict properties of both graphite and diamond well. This is due to the limited ability of EAM to describe the bare C-C interaction correctly.¹³ We note that a successful interatomic potential for an alloy system should not only predict the properties of the alloy correctly, but it should also predict the properties of the individual alloying elements in their natural crystal structures accurately. The ABOP by Henriksson et al.⁸ accurately predicts properties of cementite as well as Fe and C; however, ABOPs are not applicable to simulations involving interfaces and surfaces.¹⁴ Furthermore ABOPs are restricted to 1NN interactions only.^{14,15} Some of the more recent potentials for the Fe-C system are implemented using in-house developed molecular dynamics codes, which limits the potentials' usability by a wide scientific community.

In the present work, we developed a 2NN MEAM potential for the Fe-C alloy system that predicts the structure and properties of cementite. Our Fe-C alloy potential is based on previously developed 2NN MEAM potentials for Fe¹⁶ and C¹⁷ in their pure forms. The C MEAM potential predicts both diamond and graphite as stable structures with almost degenerate energies. Using the Fe and C single element potentials, we arrived at the best possible parameterization of the alloy potential of Fe-C for the purposes specified by the objective function which takes into account the various properties of Fe-C alloys.

II. METHODS

A. MEAM Calculations

For all atomistic simulations described in the present work, we used MEAM as implemented in LAMMPS, the classical molecular dynamics simulation code from Sandia National Laboratories.^{18,19} To compare the results of the current potential with published potentials of Refs. 12 and 8 we used the published data. For an extensive comparison of all properties of cementite with Lee's potential⁴ we obtained the LAMMPS version of the potential from the author and conducted our own calcu-

lations using LAMMPS.

B. DFT calculations

Some of the reference data required for potential construction and validation are not readily available from experiments. With respect to the Fe-C system these include the heat of formation of Fe-C in the B_1 structure, the heat of formation of Fe-C in the L_{12} structure and the interstitial energies of C in the bcc Fe lattice at octahedral and tetrahedral positions. To obtain these properties, we performed first-principles calculations using Density Functional Theory (DFT)^{20,21} with Projector Augmented Wave (PAW) pseudopotentials.²² Electron exchange and correlation were treated with the Generalized Gradient Approximation (GGA) as parameterized by Perdew et al.²³ Brillouin zone sampling was performed using the Monkhorst-Pack scheme,²⁴ with a Fermi-level smearing of 0.2 eV applied using the Methfessel-Paxton method.²⁵ Geometric optimizations were carried out using the conjugate gradient minimization method.²⁰

III. SINGLE ELEMENT POTENTIALS

The single element MEAM potential parameters used in the present work are presented in Table I. The parameters for Fe are from the MEAM potential developed by Lee et al.,¹⁶ and the parameters for C are from Uddin et al.¹⁷

1. Energy vs. volume curves

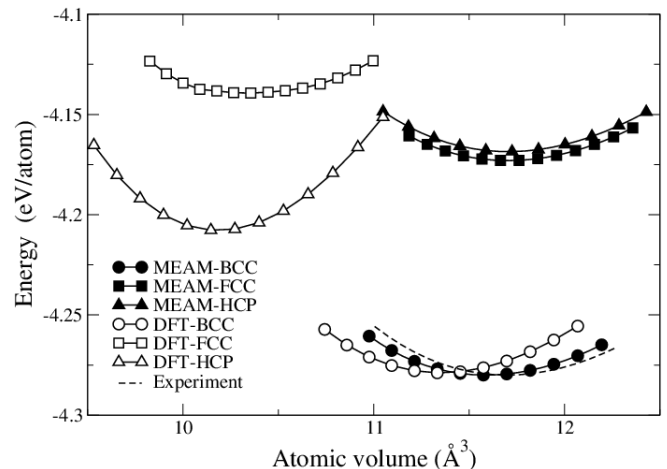


FIG. 1. Energy vs. volume curves for Fe in bcc, fcc and hcp crystal structures. The solid curve is constructed from experimental values in Table II. For ease of comparison, the DFT curves are shifted vertically by a constant amount equal to the difference between experimental and DFT cohesive energies of Fe in bcc at equilibrium volumes.

TABLE I. Set of the MEAM potential parameters for pure Fe (by Lee et al.¹⁶) and C (by Uddin et al.¹⁷). The bcc and diamond lattices are chosen as the reference structures for Fe and C, respectively. See Ref. 1 and 3 for the meaning of each parameter.

Element	E_c	r_e	r_{cut}	A	α	a_3	ρ_0	$\beta^{(0)}$	$\beta^{(1)}$	$\beta^{(2)}$	$\beta^{(3)}$	$t^{(0)}$	$t^{(1)}$	$t^{(2)}$	$t^{(3)}$	C_{min}	C_{max}
Fe	4.28	2.469	4.5	0.585	5.027	0.3	1.0	3.8	2.0	0.9	0.0	1.0	-0.8	12.3	2.0	1.9	2.8
C	7.37	1.545	4.5	1.49	4.38	0.0	1.0	4.26	5.0	3.2	3.98	1.0	7.5	1.04	-1.01	0.68	2.0

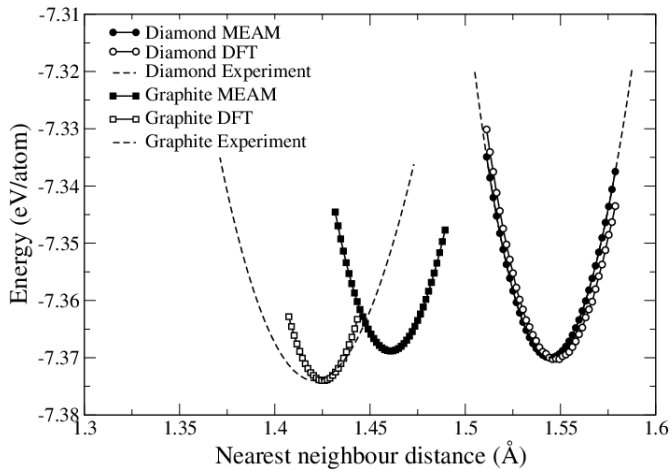


FIG. 2. Energy *vs.* nearest neighbor distance curves for C in diamond and graphite. The solid curve is constructed from experimental values in Table II. For comparison, the DFT curve is shifted vertically to the experimental cohesive energy at the equilibrium nearest neighbor distance.

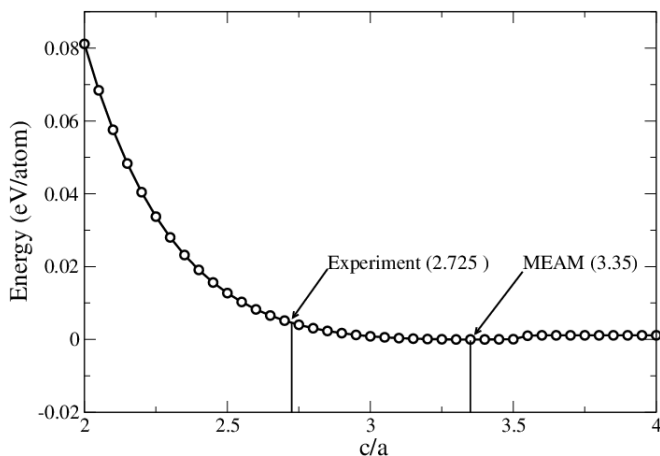


FIG. 3. Cohesive energy of graphite as a function of the c/a ratio. Energy at zero is set to the minimum energy predicted by MEAM.

Energy variation with respect to volume or nearest neighbor distance is considered an important test of validity for interatomic potentials. Here we present the energy *vs.* volume curves generated by the single element potential for Fe and energy *vs.* nearest neighbor distance curves generated by the single element potential for C. Fig. 1 shows the energy *vs.* volume curve for bcc Fe in

comparison with curves generated by DFT calculations as well as using experimental data. It is well known that DFT overestimates the cohesive energy.²⁶ Therefore, the DFT curve is shifted vertically by a constant amount to the experimental cohesive energy at the equilibrium volume to aid the comparison of the curves. Due to overbinding, the DFT's prediction for the equilibrium volume is underestimated.²⁷ Therefore, the DFT curve sits to the left of the experimental curve. The experimental curve was generated through Rose's equation of state²⁸ (Eq. (1)) using the experimental bulk modulus, cohesive energy, and atomic volume at equilibrium listed in Table II. We also tested the stability of Fe in several different crystal structures including body-centered cubic (bcc), face-centered cubic (fcc) and hexagonal closed packed (hcp) structures as shown in Fig. 1. The Fe MEAM potential correctly predicts that bcc is the most stable structure, as observed in experiment and by the first-principles methods. MEAM predicts that fcc and hcp Fe are much closer in energy and have a larger volume than that calculated from DFT.

The single-element MEAM potential for C predicts both diamond and graphite to be stable structures. Energy *vs.* nearest neighbor distance curves for diamond and graphite are shown in Fig. 2. The experimental curves were constructed from Rose's equation of state²⁸ (Eq. (1)) using the experimental bulk modulus, cohesive energy, and nearest neighbor distance at equilibrium, as listed in Table II. MEAM predictions for diamond are in good agreement with experiment. MEAM predicts almost degenerate cohesive energies for graphite and diamond, while DFT predicts graphite to be ~ 0.1 eV more stable than diamond. For graphite, DFT predicts a first-nearest neighbor (1NN) distance in good agreement with experiment, while MEAM predicts a 1NN distance $\sim 3\%$ greater than the experimental value. The experimental ratio between lattice parameters c and a in graphite (hereafter referred as c/a ratio) is 2.725.²⁹ MEAM optimized the c/a ratio of the graphite structure to 3.35. The disagreement between experimental and MEAM values for c/a ratio is due to the incorrect prediction of interlayer interaction of graphite, which is dominated by van der Waals forces that are not described by MEAM. However, the dependence of cohesive energy on the c/a ratio is small. Fig. 3 shows the change in energy as c is varied while keeping a at the MEAM optimized value. According to Fig. 3, the difference in cohesive energy of graphite between the experimental and MEAM c/a ratio is ~ 4 meV/atom. In constructing the energy *vs.* nearest

neighbor distance curves for graphite, the inter-planar distance was scaled with the lattice constant. The experimental ratio was used in the generation of the DFT curve, while the MEAM curve was constructed with the predicted c/a ratio.

2. Single element material properties

The cohesive energy, equilibrium lattice constants, and bulk moduli for bcc Fe, graphite, and diamond were determined by fitting Rose's equation of state²⁸

$$E_i^u(R) = -E_i^0 \left(1 + a^* + a_3 \frac{a^{*3}}{R/R_i^0} \right) e^{-a^*} \quad (1)$$

$$a^* = \alpha_i \left(\frac{R}{R_i^0} - 1 \right) \quad (2)$$

$$\alpha_i^2 = 9B_i\Omega_i/E_i^0 \quad (3)$$

to the energy *vs.* nearest neighbor distance/volume curves generated by MEAM. R_i^0 is the equilibrium nearest neighbor distance, E_i^0 is the cohesive energy, B_i is the bulk modulus, Ω_i is the equilibrium atomic volume and a_3 is the coefficient of the cubic term. a_3 is set to zero when fitting to energy *vs.* nearest neighbor distance/volume curves generated by MEAM. The single element material properties compared to experimental values are given in Table II.

TABLE II. Material properties predicted by the single element MEAM potentials. E_c is the cohesive energy (eV/atom); a and c are the equilibrium lattice constants (\AA); B is the bulk modulus (GPa); and Ω_0 is the equilibrium atomic volume ($\text{\AA}^3/\text{atom}$). Experimental data are given in parentheses. Experimental values for equilibrium atomic volume were calculated from the experimental lattice parameter(s).

Property	bcc Fe	diamond	graphite
E_c	-4.28 (-4.28 ^a)	-7.37 (-7.37 ^c)	-7.369 (-7.374 ^d)
B	175 (166-173 ^b)	443 (443 ^c)	176 (286 ^d)
a	2.86 (2.86 ^b)	3.567 (3.567 ^c)	2.53 (2.461 ^d)
c	—	—	8.476 (6.709 ^d)
Ω_0	11.64 (11.70)	5.67 (5.67)	11.75 (8.80)

^a Ref. 30 as reported by Lee et al.¹⁶

^b As reported by Lee et al.¹⁶

^c Refs. 31 and 32 as reported by Fahy et al.³³

^d Refs. 34 and 35 as reported by Yin et al.²⁹

IV. CONSTRUCTION OF FE-C ALLOY POTENTIAL

Table III lists the parameters in the 2NN MEAM potential for Fe-C alloy system optimized by following the general framework developed by Tschopp et al.³⁶ The

framework consists of two stages. The first stage, called the Global Approach (GA), is a coarse refinement of the parameter space of the MEAM potential, which initializes the MEAM potential parameters and performs a sensitivity analysis for the parameters. The second stage, called the Local Approach (LA), evaluates the sensitive parameters sampling the parameter space with a stratified sampling method and generates analytical models for design optimization of the potential.

In the GA stage, a coarse refinement of the parameter space is performed using a partial set of the properties in the objective function including: the heats of formation of cementite, Fe_3C in L_{12} structure and FeC in B_1 structure, and the interstitial energies of C in the bcc Fe lattice at octahedral and tetrahedral positions. The potential parameters were initialized as specified by the MEAM formulation.^{1,3} α defined by Eq. (3) and r_e (equilibrium nearest neighbor distance) are determined by the reference structure properties. For the present case, FeC in L_{12} structure is used as the reference structure and the values predicted by DFT are used to set α and r_e since experimental values are not available for this hypothetical structure. Parameters α and r_e remain unchanged throughout the optimization process since they are defined by the MEAM formulation. Next, a sensitivity analysis was performed to evaluate the influence of each parameter on the properties. This step helps identify parameters with the most significant effect on the selected target properties of the Fe-C system. By identifying the parameters that have the most influence on the properties of the Fe-C system we are able to reduce the number of parameters to be included in the later stages. For the present case, the GA stage identified five parameters— Δ , a_3 , $\rho_0(\text{C})$, $C_{\min}(\text{Fe,Fe,C})$, and $C_{\min}(\text{C,C,Fe})$ —to be sufficiently sensitive to be further explored in the LA stage of the optimization. Parameters that are deemed insensitive are fixed at the default values recommended in the MEAM formulation.

The LA stage of the potential optimization procedure involves sampling the bounded potential parameter space, generating analytical models that represent the nonlinear correlations between the potential parameters, and using an objective function to converge on the required parameterization of the potential. A stratified random sampling method known as Latin Hypercube Sampling (LHS)³⁷ was used to sample the potential parameter space with 4000 different potential parameter combinations. The set of properties chosen for the Fe-C system are calculated for each parameter combination. This is the most computationally-intensive step of the potential fitting process. Using the data from the parameter space sampling step, analytical models representing the relationship between potential parameters and the selected target properties are generated. This is done by fitting higher-order polynomial regression models to the sampled data. The analytical models represent a response surface for the sensitive potential parameters. At this stage of the optimization an objective function repre-

TABLE III. The optimized parameters in the 2NN MEAM potential for Fe–C alloy system. The triplet (A,B,C) represents the configuration with C atom in between A and B atoms. The B_1 lattice is chosen as the reference structure.

Parameter	Value
Δ	0.002
r_e	1.92
r_{cut}	4.5
α	4.75
a_3	0.125
$\rho_0(\text{Fe})$	1.0
$\rho_0(\text{C})$	5.49
$C_{\text{max}}(\text{Fe,Fe,C})$	2.8
$C_{\text{max}}(\text{Fe,C,C})$	2.8
$C_{\text{max}}(\text{Fe,C,Fe})$	2.8
$C_{\text{max}}(\text{C,C,Fe})$	2.8
$C_{\text{min}}(\text{Fe,Fe,C})$	0.06
$C_{\text{min}}(\text{Fe,C,C})$	2.0
$C_{\text{min}}(\text{Fe,C,Fe})$	2.0
$C_{\text{min}}(\text{C,C,Fe})$	0.5

senting all of the interested properties of the Fe–C system is introduced. The objective function is constructed by combining the weighted differences between the MEAM predicted values and the target values of the chosen properties. Target values are set to experimental values when available or DFT values otherwise. Then a constrained nonlinear optimization procedure is used to evaluate the analytical models by minimizing the objective function.

The properties included in the objective function are the properties of cementite (equilibrium lattice parameters and volume, heat of formation, elastic constants, and surface formation energies); properties of Fe_3C in L_{12} structure (heat of formation and equilibrium volume); properties of FeC in B_1 structure (heat of formation, equilibrium volume and elastic constants) and interstitial defect energies of C in the bcc Fe lattice at octahedral and tetrahedral positions. The weighting factors of the objective function balance the trade-offs in potential optimization. The purpose of the present work is to model the properties of cementite while reproducing the Fe–C alloy system properties to an acceptable accuracy. This is realized by choosing weighting factors in a way that cementite properties were prioritized first, then the interstitial defect energies, and then the properties of hypothetical structures B_1 and L_{12} . By varying the weights, the objective function is changed and the constrained nonlinear optimization procedure can traverse the response surface represented by the analytical models to obtain a final set of potential parameters. For each set of weighting factors a potential is generated. By using a matrix of weighting factors with the required prioritization of the target properties, we were able to minimize the objective function and arrive at the set of optimal potential parameters in Table III. The optimized potential is then validated by predicting material properties that were not used in the optimization procedure. We used the melting

temperature of cementite to validate the potential and its prediction is explained in Sec. VIII. Table IV shows the material properties predicted by the present MEAM potential compared with DFT/experimental data and the values from other existing potentials.

V. STRUCTURAL AND ELASTIC PROPERTIES OF CEMENTITE

Structural properties of cementite including the equilibrium lattice parameters, the equilibrium volume per atom, and the heat of formation are presented in Table IV with comparison to DFT/experiment, and other interatomic potentials. Our prediction of the heat of formation of cementite is in good agreement with DFT and experimental data. Lee’s and Henriksson’s potentials also predict values in good agreement with DFT and experiment, while Ruda’s potential predicts a much larger value. Lattice constants of the present MEAM and literature potentials^{4,8,12} agree well with experiment, while DFT predicts lower values. As a test of validity, the variation of cohesive energy with volume was calculated. Fig. 4 compares the energy *vs.* volume curves for cementite generated by the present MEAM potential with DFT and experimental curves. During volume variation of cementite, the ratios between a , b and c lattice parameters were held constant. As noted before, DFT overestimates the cohesive energy and underestimates the equilibrium volume. Therefore, the DFT curve sits to the left of the experimental curve, and it is shifted vertically to the experimental cohesive energy at the equilibrium volume to aid the comparison. The experimental curve was generated by Murnaghan’s equation of state^{35,46}

$$E(V) = E(V_0) + \frac{B_0 V}{B'_0(B'_0 - 1)} \times \left[B'_0 \left(1 - \frac{V_0}{V} \right) + \left(\frac{V_0}{V} \right)^{B'_0} - 1 \right]. \quad (4)$$

with the experimental bulk modulus B_0 ⁴⁰, its derivative B'_0 ⁴⁰, volume V_0 ⁴³, and cohesive energy $E(V_0)$.⁶ The experimental single-crystal bulk modulus of cementite has not yet been determined; therefore, the polycrystalline bulk modulus of cementite was used to generate the experimental curve.

A. Single-Crystal Elastic Properties

The elastic moduli of cementite were calculated and compared to DFT and the interatomic potentials by Ruda et al.,¹² and Henriksson et al.⁸ as presented in Table IV. They were calculated using the deformation matrix presented in Jiang et al.³⁹ In linear elastic theory, deformation energy is a function of strain. Distortion energies (ΔE) calculated for strains (δ) equal to $\pm 0.5\%$ were fitted to $\Delta E = k_2 \delta^2 + k_3 \delta^3$. DFT calculations

TABLE IV. Comparison of the present MEAM potential with DFT/experimental data and potentials by Lee⁴, Ruda et al.¹² and Henriksson et al.⁸ ΔH_f is the heat of formation, Ω_0 is the equilibrium volume, B is polycrystalline bulk modulus, G is polycrystalline shear modulus, Y is polycrystalline Young's modulus and ν is polycrystalline Poisson's ratio.

Properties	DFT/Expt.	MEAM	Lee ⁴	Ruda ¹²	Henriksson ⁸
Cementite					
ΔH_f (eV/atom)	0.01 (0.05 ^a)	0.06	0.02 ⁱ , -0.015 ^j	0.18	0.03
Ω_0 ($\text{\AA}^3/\text{atom}$)	9.56 ^b (9.67 ^l)	9.49	9.50	9.11	9.33
Lattice parameters (\AA)					
a	5.06 ^b (5.08 ^l)	5.05	5.16	5.14	5.09
b	6.70 ^b (6.73 ^l)	6.69	6.32	6.52	6.52
c	4.51 ^b (4.52 ^l)	4.49	4.66	4.35	4.50
Elastic constants (GPa)					
C_{11}	388 ^c	322		263	363
C_{22}	345 ^c	232		219	406
C_{33}	322 ^c	326		247	388
C_{12}	156 ^c	137		176	181
C_{23}	162 ^c	118		143	130
C_{13}	164 ^c	170		146	166
C_{44}	15 ^c	17		77	91
C_{55}	134 ^c	103		95	125
C_{66}	134 ^c	64		123	134
Polycrystalline moduli					
B (GPa)	224 (174 \pm 6 ^d)	188		183	234
G (GPa)	72 (74 ^e)	56		69	114
Y (GPa)	194 (177 ^f , 196 ^g , 200 ^e)	153		184	293
ν	0.36 (0.36 ^e)	0.36		0.33	0.29
Surface energies (J/m ²)					
$E_{(001)}$	2.05 ^h	2.05		1.96	
$E_{(010)}$	2.26 ^h	1.80		2.00	
$E_{(100)}$	2.47 ^h	2.01		2.34	
Interstitial Energies (eV)					
$E_{\text{Tetrahedral}}$	2.14	1.76		2.08	1.50
$E_{\text{Octahedral}}$	1.25	1.55		1.81	1.18
Hypothetical structures					
$\Delta H_f B_1$ (eV/atom)	0.53	0.002			
$\Omega_0 B_1$ ($\text{\AA}^3/\text{atom}$)	7.97	7.08	8.49		
$\Delta H_f L_{12}$ (eV/atom)	0.72	0.66			
$\Omega_0 L_{12}$ ($\text{\AA}^3/\text{atom}$)	10.27	10.05			
B_1 elastic constants (GPa)					
C_{11}	601	566	550 ^k		
C_{12}	589	213	228 ^k		
C_{44}	83	145	33 ^k		

^a Meschel et al.⁶

^b Shein et al.³⁸

^c Data from relaxed calculations done by Jiang et al.³⁹

^d Li et al.⁴⁰

^e Laszlo et al.⁴¹

^f Mizubayashi et al.⁴²

^g Umemoto et al.⁴³

^h Chiou et al.⁴⁴

ⁱ B.-J Lee⁴

^j Fang et al.⁵

^k Private communication with B.-J. Lee

^l Wood et al.⁴⁵ as cited by Shein et al.³⁸

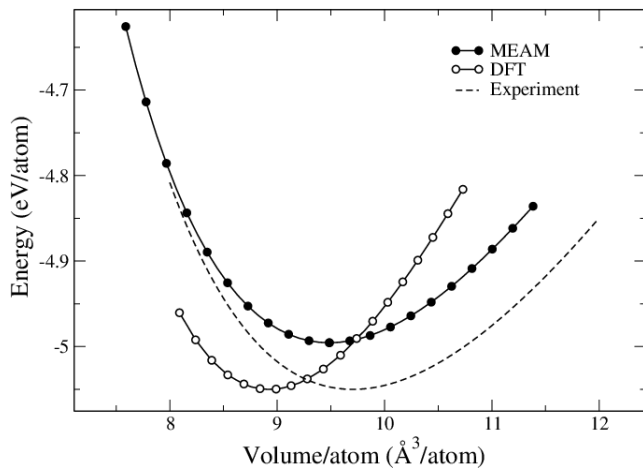


FIG. 4. Comparison of energy *vs.* volume curves for cementite. The dashed-line curve is constructed from experimental values of the cohesive energy, equilibrium volume and polycrystalline bulk modulus, of cementite. For comparison, the DFT curve is shifted vertically to the experimental cohesive energy at the equilibrium volume.

were performed for $\delta = \pm 2\%$.³⁹ The single-crystal elastic constants were obtained using the relationships for the quadratic coefficient k_2 listed in Jiang et al.³⁹ These results show that the present MEAM potential for Fe–C alloy predicts cementite to be stable (positive elastic constants) and their values are reasonably close to those predicted by DFT. Specifically, the present MEAM potential reproduces the low value of c_{44} reported by DFT, which none of the other interatomic potentials were able to do (MEAM c_{44} of 17 GPa vs DFT c_{44} 15 GPa).

B. Polycrystalline Elastic Properties

Theoretical upper and lower bounds for the polycrystalline bulk modulus (B) and shear modulus (G) were calculated using the single-crystal elastic constants according to methods by Reuss and Voigt.^{39,47} The polycrystalline B and G were then estimated using Hill’s average.^{39,48} Young’s modulus (Y) and Poisson’s ratio (ν) were calculated by using:³⁹

$$Y = 9BG/(3B + G) \quad (5)$$

$$\nu = (3B/2 - G)/(3B + G). \quad (6)$$

Polycrystalline elastic moduli predicted by the present MEAM potential are presented in Table IV, in comparison with DFT, experiment, and interatomic potentials by Ruda et al.,¹² and Henriksson et al.⁸ The elastic constants predicted by DFT are in good agreement with experiment. The present MEAM potential gives the best agreement with experiment among the three interatomic potentials for B and ν ; the present MEAM predicts the ν value equal to the experimental value. Ruda’s potential predicts the best agreement with experiment for G and Y .

C. Surface Energies

Calculations were performed on (001), (010), and (100) surfaces to determine the surface formation energy. Table IV compares the surface formation energies of the present MEAM to DFT⁴⁴ and the interatomic potential by Ruda et al.¹² The atoms near the surfaces are fully relaxed to allow reconstruction if necessary. The predicted surface energies have the same order of magnitude as DFT results. However, the present MEAM gives a wrong order of stability among the three surfaces.

VI. INTERSTITIAL ENERGIES

The interstitial point defect formation energy E_f^{int} is given by

$$E_f^{\text{int}} = E_{\text{tot}}[N + A] - E_{\text{tot}}[N] - \epsilon_A \quad (7)$$

where the total energy of a system with N (Fe or C) atoms is $E_{\text{tot}}[N]$ and $E_{\text{tot}}[N + A]$ is the total energy of a system with N atoms plus the inserted atom A (Fe or C), and ϵ_A is the total energy per atom of type- A in its most stable bulk structure. In this case, we considered interstitial defects of C atoms in a Fe bcc lattice. Interstitial defect formation energies of C at the octahedral and tetrahedral positions of the Fe bcc lattice were calculated. The results are presented in Table IV with comparison to DFT results, and to other interatomic potentials. The present MEAM potential predicts the octahedral defect to be the most stable in agreement with DFT results. However, the difference between two defect energies is smaller compared to that of DFT.

VII. PROPERTIES OF HYPOTHETICAL CRYSTAL STRUCTURES

Heat of formation of Fe–C in B_1 crystal structure and L_{12} crystal structure as well as their equilibrium volumes are also presented in Table IV. The heat of formation of B_1 is unusually low compared to DFT results. B_1 is the reference structure of the Fe–C alloy potential and its heat of formation is defined by the Δ parameter of the potential. The Δ parameter also has a large effect on the heat of formation of cementite and thereby to its structural and elastic properties. Heat of formation of B_1 and L_{12} were used as target properties in the GA stage of the potential construction process. However the heat of formation of these two structures were weighted far less in the construction of the objective function for obtaining the final potential parameters as compared to properties of cementite. This caused the Δ parameter to have a low value to reproduce overall cementite properties with greater accuracy. This should not pose a serious problem since B_1 is a hypothetical structure.

1. Energy vs. volume curves for B_1 and L_{12} structures

The cohesive energy of Fe–C in the B_1 and L_{12} crystal structures as a function of the atomic volume is shown in Figs. 5 and 6, respectively. For the B_1 structure, the present MEAM potential predicts an atomic volume $\sim 11\%$ less, and a bulk modulus $\sim 0.3\%$ less than DFT. The MEAM prediction for the L_{12} structure gives an atomic volume $\sim 11\%$ greater, and a bulk modulus 35% less than DFT. As mentioned earlier, DFT overestimates the cohesive energy. Therefore, to aid the comparison in these figures, the DFT curves are shifted vertically by constant amounts to the MEAM-predicted cohesive energies at the equilibrium nearest neighbor distances.

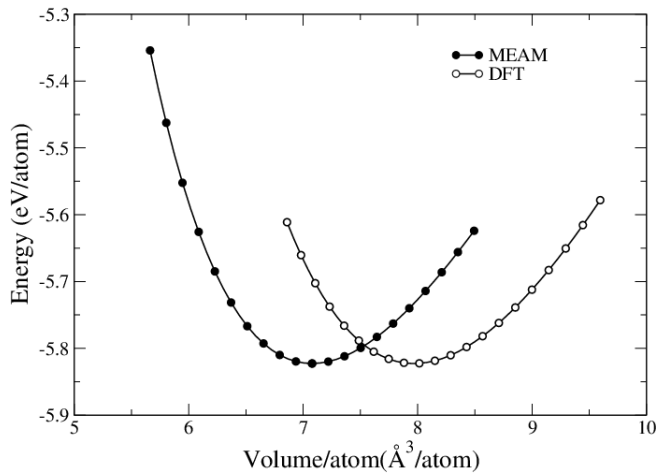


FIG. 5. Comparison of the energy *vs.* volume curves of Fe–C alloy system in the B_1 structure. DFT curve is shifted vertically to the MEAM-predicted cohesive energy at the equilibrium nearest neighbor distance to aid the comparison with the MEAM curve.

2. Elastic constants of FeC in the B_1 crystal structure

Elastic constants of Fe–C in the B_1 crystal structure were calculated using the Fe–C MEAM potential and are listed in Table IV in comparison with DFT calculations and the interatomic potential by Lee.⁴ They were calculated using the deformation matrix presented by Jiang et al.³⁹ Distortion energies (ΔE) calculated for strains (δ) equal to $\pm 0.1\%$ were fitted to $\Delta E = k_2\delta^2 + k_3\delta^3$. The result from the present work for C_{11} compares reasonably well with the DFT result. C_{12} is predicted at a lower value than DFT, but it is in the same order of magnitude. MEAM prediction of C_{44} is significantly larger than the DFT result.

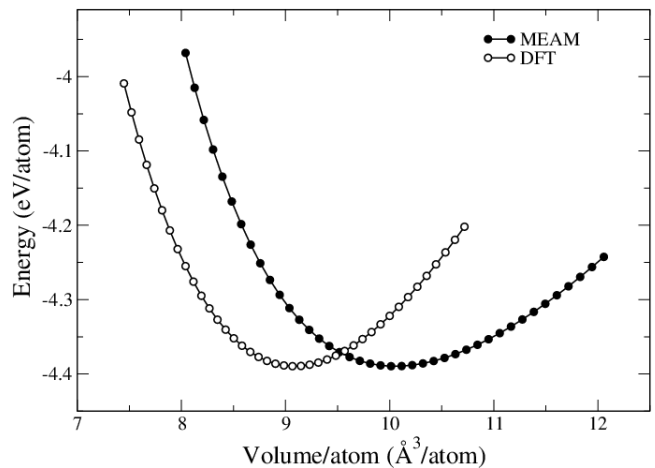


FIG. 6. Comparison of the energy *vs.* volume curves of Fe–C alloy system in the L_{12} structure. DFT curve is shifted vertically to the MEAM-predicted cohesive energy at the equilibrium nearest neighbor distance aid the comparison with the MEAM curve.

VIII. THERMAL PROPERTIES OF CEMENTITE

A. Thermal stability of cementite

The stability of cementite at high temperatures was investigated through molecular dynamics (MD) simulations in a canonical (NVT) ensemble from temperatures ranging from 300 K to 1400 K. At the end of these MD simulations, cementite retained its crystalline structure, affirming its stability at high temperatures. The present Fe–C MEAM potential was also used to predict several thermal properties of cementite. In this section, we present calculations for predicting melting temperature and variation of specific heat and volume of cementite with respect to temperature.

B. Melting temperature simulation

Cementite does not have a well-defined melting temperature due to its metastable nature.⁸ Experimentally, cementite decomposes to ferrite (bcc Fe) and graphite if heated for between 923 K and 973 K for several years.⁷ The Fe–C phase diagram also has well-defined eutectic point at 1420 K,^{7,49} where liquid consisting of Fe and C austenite (fcc Fe) and cementite co-exists in equilibrium. Above 1420 K the phase diagram for cementite is determined through mathematical calculations.⁴⁹ For the purpose of this calculation, we considered the melting temperature of cementite to be the temperature when cementite loses its crystal structure and becomes a random collection of Fe and C atoms. The melting temperature calculation can be done using a single-phase simulation box. However, the single phase method generally overes-

timates the melting temperature due to the lack of the interface effects.⁵⁰ To avoid this superheating problem and predict the melting temperature more accurately, we used a two-phase simulation box that contains both solid and liquid phases.

1. Preparation of two-phase simulation box

We performed two-phase simulations (TPS) in the isothermal-isobaric (NPT) ensemble to determine the melting temperature of cementite. The simulation box contained both solid and liquid phases of cementite. First a supercell containing $14 \times 7 \times 7$ unit cells of cementite (10976 atoms) was heated via MD runs in the NPT ensemble with $T = 1200$ K and $P = 0$. Next, one half of the atoms in the supercell were fixed in their positions and MD runs were carried out for the other half in the NPT ensemble with a sufficiently high temperature (such as $T = 4000$ K) and $P = 0$ to create a liquid phase. The resulting supercell was then subjected to MD runs in the NPT ensemble with $T = 1500$ K (which is higher than the expected melting temperature) and $P = 0$, still keeping the same half of the atoms fixed. The result of this process was a supercell containing solid cementite at 1200 K in one half, and liquid cementite at 1500 K in the other. This ensures a minimum difference of stress between atoms in liquid and solid phases of the supercell. This supercell was then used in the simulations of solidification and melting of cementite.

2. Two-phase simulation

The two-phase supercell prepared in the previous section was heated by MD runs in the NPT ensemble where the temperature T was increased from 1000 K to 1500 K in 100 K intervals. Each system ran for 1.6 ns of simulation time at a time step of 2 fs. The phase change of the two-phase simulation box was visually monitored. At 1400 K the solid phase of the simulation box progressed to occupy the entire box. In comparison, at 1500 K the liquid phase of the simulation box progressed to occupy the entire box. Next, the initial two-phase simulation box was heated from 1400 K to 1500 K in 10 K intervals using NPT MD runs. Each system was equilibrated for at least 5×10^6 time steps totaling to 10 ns. The final state of the system was visually inspected. If the final state appeared to have both liquid and solid phases, more MD runs were performed until the final state of the supercell contained only one phase. Some systems required as much as 32 ns of MD runs to arrive at a single phase. The transformation of the two-phase simulation box to a one-phase simulation box near the predicted melting temperature is presented in Fig. 7 and Fig. 8. The total energy, volume, and pressure of the systems were determined through averaging the values of the final 40 000 time steps (80 ps) of each simulation.

In Fig. 9 we plot the total energy, volume, specific heat, and the derivative of volume as functions of temperature. Experimental data for specific heat and volume are not available for the 1400-1500 K temperature range. Available experimental data are the heat capacity of $3.6 k_B/\text{atom}$ at 1023 K,⁵¹ and the experimental volume of $10 \text{ \AA}^3/\text{atom}$ at 1070 K.⁵² Specific heat and volume determined by Dick et al. from the first-principles calculations⁵³ done on the solid phase of cementite are included for comparison in Figs. 9(b) and (c). Since Dick and coworkers used a single-phase simulation box, their simulation clearly shows superheating causing the melting temperature to be overestimated. This can be attributed to the absence of the solid-liquid interface in single phase simulations. In Fig. 9(c) the specific heat shows a peak between 1420 K and 1430 K. Therefore we assign 1425 ± 5 K as the melting temperature of cementite. This is a reasonable prediction compared to experimental eutectic point at 1420 K.^{7,49}

IX. SUMMARY AND CONCLUSION

In this study, we investigated the properties of cementite using an interatomic potential developed within the MEAM formalism. Previously developed single-element interatomic potentials for Fe and C were used to develop the Fe-C alloy MEAM potential. The single-element potential for C predicts graphite and diamond as stable structures with nearly degenerate energies. MEAM potentials for pure elements predict the heat of formation, bulk moduli, and lattice constants of Fe and C in their natural crystal structures in good agreement with experimental data. The alloy potential for the Fe-C system was developed primarily to reproduce structural and elastic properties of cementite. Secondly, the interstitial energies of C in bcc Fe, as well as heats of formation of Fe-C alloys in B_1 and L_{12} structures were included with less weighting factors. The constructed potential was used to predict structural, elastic, and thermal properties of cementite. Structural properties tested included the heat of formation, the equilibrium lattice constants, the equilibrium volume, and the energy variation with respect to volume. MEAM predictions are in good agreement with DFT and experiment. Nine single-crystal elastic constants were calculated and used to estimate polycrystalline bulk modulus, shear modulus, Young's modulus, and Poisson's ratio of cementite. Surface energies for (001), (010), and (100) surfaces were also calculated and compared. The potential was validated by predicting the thermal stability of cementite, its melting temperature and the variation of specific heat and volume of cementite with respect to temperature by two-phase (solid/liquid) MD simulations. The present MEAM potential predicted the melting temperature of cementite to be 1425 ± 5 K.

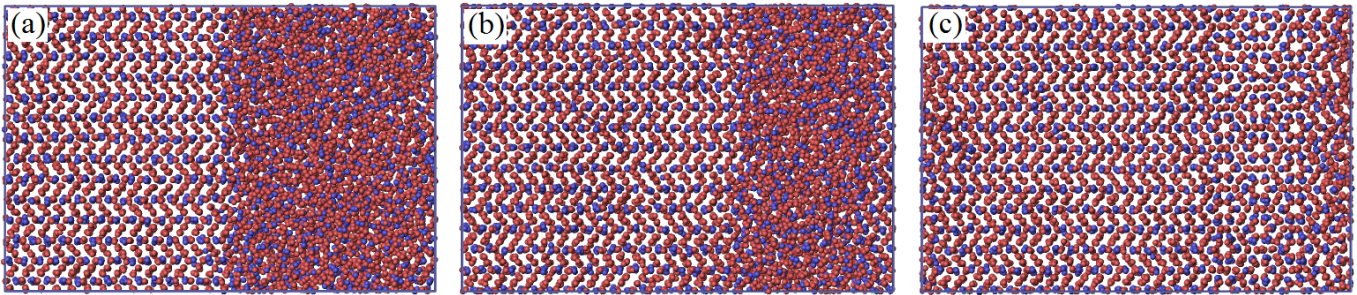


FIG. 7. (Color online) Snapshots of the two-phase MD simulation in the NPT ensemble with $T = 1420$ K and $P = 0$. Red spheres are Fe atoms and blue spheres are C atoms. (a) Initial state of the simulation box, which contains both liquid and solid phases of cementite. (b) Intermediate state of the simulation box at 16 ns, as the solid phase propagates to the liquid phase. (c) Final state of the simulation box at 32 ns, when the entire system has turned into a solid phase.

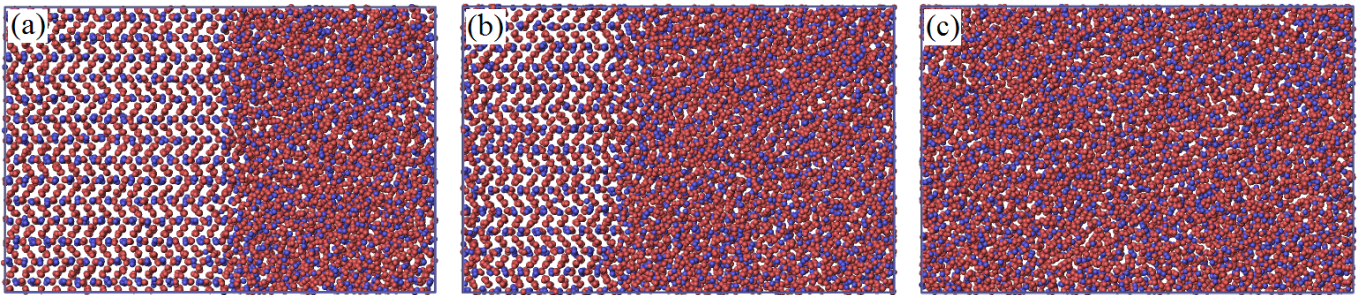


FIG. 8. (Color online) Snapshots of the two-phase MD simulation in the NPT ensemble with $T = 1430$ K and $P = 0$. Red spheres are Fe atoms and blue spheres are C atoms. (a) Initial state of the simulation box, which contains both liquid and solid phases of cementite. (b) Intermediate state of the simulation box at 20 ns, as the liquid phase propagates to the solid phase. (c) Final state of the simulation box at 30 ns, when the entire system has turned into a liquid phase.

X. ACKNOWLEDGMENTS

We are grateful to A.B. Belonoshko for his suggestions in conducting the two-phase melting simulations. This work was supported in part by the Department of

Energy, grants DE-EE0002323 and DE-FC26-06NT2755. Computer time allocation has been provided by the High Performance Computing Collaboratory (HPC²) at Mississippi State University.

* Author to whom correspondence should be addressed; kimsg@ccs.msstate.edu

¹ M. I. Baskes, Phys. Rev. B **46**, 2727 (1992).

² M. S. Daw and M. I. Baskes, Phys. Rev. B **29**, 6443 (1984).

³ B.-J. Lee, M. Baskes, H. Kim, and Y. K. Cho, Phys. Rev. B **64**, 184102 (2001).

⁴ B. Lee, Acta Materialia **54**, 701 (2006).

⁵ C. M. Fang, M. A. van Huis, B. J. Thijsse, and H. W. Zandbergen, Phys. Rev. B **85**, 054116 (2012).

⁶ S. Meschel and O. Kleppa, Journal of Alloys and Compounds **257**, 227 (1997).

⁷ W. Callister and D. Rethwisch, *Materials science and engineering: an introduction*, 7th ed. (Wiley New York, 2007) pp. 290–293.

⁸ K. Henriksson and K. Nordlund, Physical Review B **79**, 144107 (2009).

⁹ C. Becquart, J. Raulot, G. Bencteux, C. Domain, M. Perez, S. Garruchet, and H. Nguyen, Computational Materials Science **40**, 119 (2007).

¹⁰ T. T. Lau, C. J. Först, X. Lin, J. D. Gale, S. Yip, and K. J. V. Vliet, Phys. Rev. Lett. **98**, 215501 (2007).

¹¹ D. J. Hepburn and G. J. Ackland, Phys. Rev. B **78**, 165115 (2008).

¹² M. Ruda, D. Farkas, and G. Garcia, Computational Materials Science **45**, 550 (2009).

¹³ A. I. Duff and M. H. F. Sluiter, MATERIALS TRANSACTIONS **51**, 675 (2010).

¹⁴ P. Erhart, N. Juslin, O. Goy, K. Nordlund, R. Mller, and K. Albe, Journal of Physics: Condensed Matter **18**, 6585 (2006).

¹⁵ K. Albe, K. Nordlund, and R. S. Averback, Phys. Rev. B **65**, 195124 (2002).

¹⁶ T. Lee, M. I. Baskes, S. M. Valone, and J. D. Doll, Journal of Physics: Condensed Matter **24**, 225404 (2012).

¹⁷ J. Uddin, M. I. Baskes, S. G. Srinivasan, T. R. Cundari, and A. K. Wilson, Phys. Rev. B **81**, 104103 (2010).

¹⁸ S. Plimpton, Journal of Computational Physics **117**, 1 (1995).

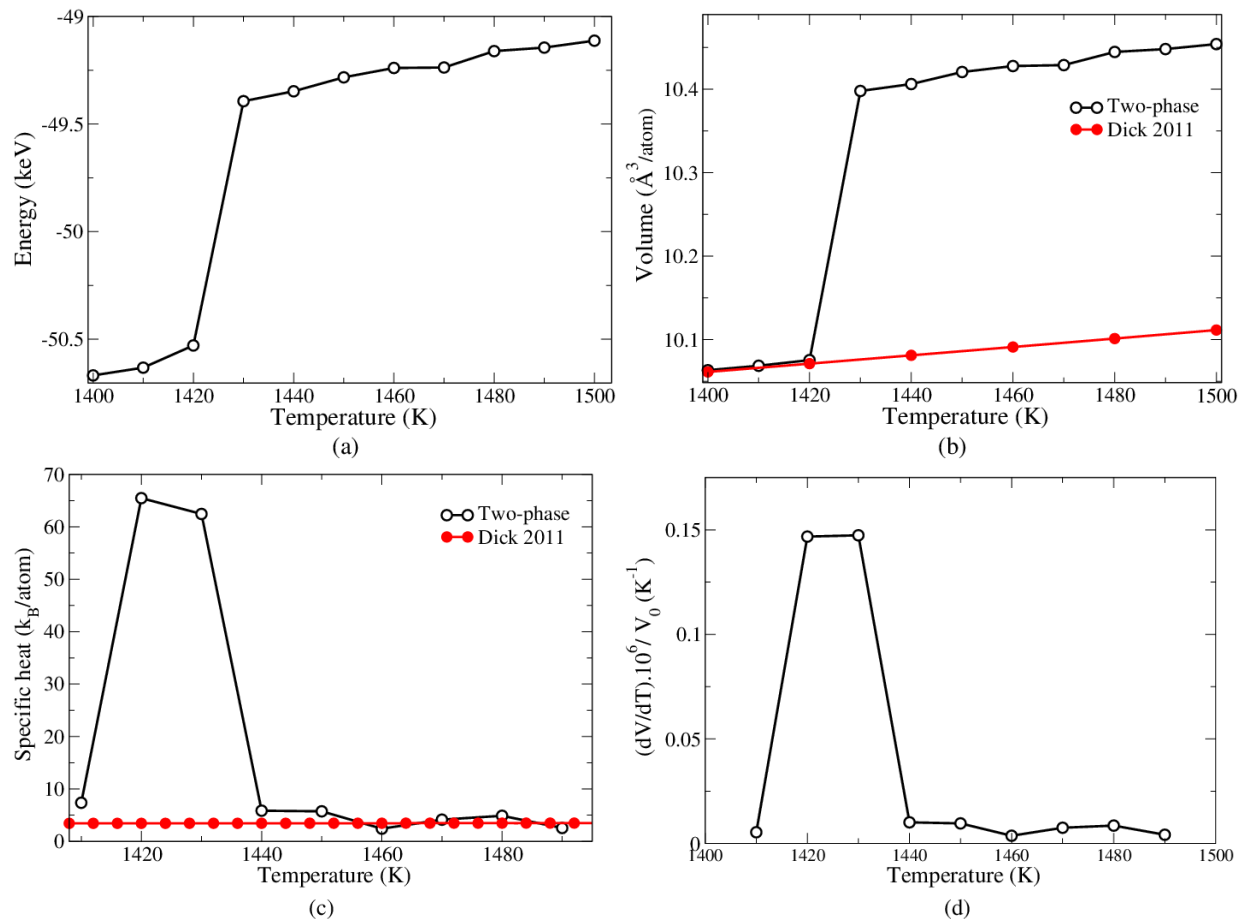


FIG. 9. Variation of properties of the two-phase system over the temperature. (a) Total energy of the system. (b) (Color online) Volume of the system. Red curve is first-principles data by Dick et al.⁵³ (c) (Color online) Specific heat of the system. Red curve is the first-principles data. (d) dV/dT of the system.

- ¹⁹ S. Plimpton *et al.*, “Lammps-large-scale atomic/molecular massively parallel simulator,” April 2011 version.
- ²⁰ G. Kresse and J. Hafner, Phys. Rev. B **47**, 558 (1993).
- ²¹ G. Kresse and J. Furthmüller, Phys. Rev. B **54**, 11169 (1996).
- ²² G. Kresse and D. Joubert, Phys. Rev. B **59**, 1758 (1999).
- ²³ J. P. Perdew, K. Burke, and M. Ernzerhof, Phys. Rev. Lett. **77**, 3865 (1996).
- ²⁴ H. Monkhorst and J. Pack, Phys. Rev. B **13**, 5188 (1976).
- ²⁵ M. Methfessel and A. T. Paxton, Phys. Rev. B **40**, 3616 (1989).
- ²⁶ P. H. T. Philipsen and E. J. Baerends, Phys. Rev. B **54**, 5326 (1996).
- ²⁷ A. Devey and N. H. de Leeuw, Phys. Rev. B **82**, 235112 (2010).
- ²⁸ J. H. Rose, J. R. Smith, F. Guinea, and J. Ferrante, Phys. Rev. B **29**, 2963 (1984).
- ²⁹ M. T. Yin and M. L. Cohen, Phys. Rev. B **29**, 6996 (1984).
- ³⁰ C. Kittel, *Introduction to Solid State Physics*, 6th ed. (John Wiley & Sons, Inc., New York, 1986).
- ³¹ J. Donohue, *The structures of the elements* (R.E. Krieger Pub. Co., Malabar, Fla., 1982) p. 256.
- ³² H. J. McSkimin, J. P. Andreatch, and P. Glynn, Journal of Applied Physics **43**, 985 (1972).
- ³³ S. Fahy and S. G. Louie, Phys. Rev. B **36**, 3373 (1987).
- ³⁴ L. Orson and Anderson, Journal of Physics and Chemistry of Solids **27**, 547 (1966).
- ³⁵ F. D. Murnaghan, Proceedings of the National Academy of Science **30**, 244 (1944).
- ³⁶ M. Tschopp, K. Solanki, M. Baskes, F. Gao, X. Sun, and M. Horstemeyer, Journal of Nuclear Materials **425**, 22 (2012).
- ³⁷ M. McKay, R. Beckman, and W. Conover, Technometrics **42**, 55 (2000).
- ³⁸ I. Shein, N. Medvedeva, and A. Ivanovskii, Physica B: Condensed Matter **371**, 126 (2006).
- ³⁹ C. Jiang, S. G. Srinivasan, A. Caro, and S. A. Maloy, Journal of Applied Physics **103**, 043502 (2008).
- ⁴⁰ J. Li, H. K. Mao, Y. Fei, E. Gregoryanz, M. Eremets, and C. S. Zha, Physics and Chemistry of Minerals **29**, 166 (2002), 10.1007/s00269-001-0224-4.
- ⁴¹ F. Laszlo and H. Nolle, Journal of the Mechanics and Physics of Solids **7**, 193 (1959).
- ⁴² H. Mizubayashi, S. Li, H. Yumoto, and M. Shimotomai, Scripta Materialia **40**, 773 (1999).
- ⁴³ M. Umemoto, Z. Liu, K. Masuyama, and K. Tsuchiya, Scripta Materialia **45**, 391 (2001).
- ⁴⁴ W. Chiou, Surface Science **530**, 87 (2003).
- ⁴⁵ I. G. Wood, L. Vočadlo, K. S. Knight, D. P. Dobson, W. G. Marshall, G. D. Price, and J. Brodholt, Journal of Applied

- Crystallography **37**, 82 (2004).
- ⁴⁶ F. Murnaghan, *Finite deformation of an elastic solid* (Dover New York, 1967).
- ⁴⁷ K. Panda and K. R. Chandran, *Acta Materialia* **54**, 1641 (2006).
- ⁴⁸ R. Hill, *Proceedings of the Physical Society. Section A* **65**, 349 (1952).
- ⁴⁹ H. Okamoto, *Journal of Phase Equilibria* **13**, 543 (1992), 10.1007/BF02665767.
- ⁵⁰ A. B. Belonoshko, *Geochimica et Cosmochimica Acta* **58**, 4039 (1994).
- ⁵¹ G. Naeser, *Mitt. Kais.-Wilh.-Inst. Eisenforsch* **16**, 207 (1934), as reported in Dick et al.⁵³.
- ⁵² R. C. Reed and J. H. Root, *Scripta Materialia* **38**, 95 (1997), as reported by Dick et al.⁵³.
- ⁵³ A. Dick, F. Körmann, T. Hickel, and J. Neugebauer, *Phys. Rev. B* **84**, 125101 (2011).